PHOTONICS Research

Mid-infrared active metasurface based on Si/VO_2 hybrid meta-atoms

Tongtong Kang,[1,2,†] Boyu Fan,[3,†] Jun Qin,[1,2] Weihao Yang,[1,2] Shuang Xia,[1,2] Zheng Peng,[1,2] Bo Liu,[4,5] Sui Peng,[4,5] Xiao Liang,[4,5] Tingting Tang,[4,5] Longjiang Deng,[1,2] Yi Luo,[6] Hanbin Wang,[6,7] Qiang Zhou,[3] and Lei Bi[1,2,*]

[1]National Engineering Research Center of Electromagnetic Radiation Control Materials, University of Electronic Science and Technology of China, Chengdu 610054, China
[2]State Key Laboratory of Electronic Thin-Films and Integrated Devices, University of Electronic Science and Technology of China, Chengdu 610054, China
[3]Institute of Fundamental and Frontier Sciences, University of Electronic Science and Technology of China, Chengdu 610054, China
[4]College of Optoelectronic Engineering, Chengdu University of Information Technology, Chengdu 610225, China
[5]State Key Laboratory of Vanadium and Titanium Resources Comprehensive Utilization, Panzhihua 617000, China
[6]Microsystem & Terahertz Research Center, China Academy of Engineering Physics (CAEP), Chengdu 610200, China
[7]Institute of Electronic Engineering, China Academy of Engineering Physics (CAEP), Mianyang 621900, China
*Corresponding author: bilei@uestc.edu.cn

Received 14 October 2021; revised 18 November 2021; accepted 22 November 2021; posted 24 November 2021 (Doc. ID 445571); published 14 January 2022

Active metasurfaces whose optical properties can be tuned by an external stimulus have attracted great research interest recently. Introduction of VO_2 phase change material in all-dielectric metasurfaces has been demonstrated to modulate the resonance wavelength and amplitude in the visible to near-infrared wavelength range. In this study, we report a mid-infrared active metasurface based on Si/VO_2 hybrid meta-atoms. By incorporating VO_2 thin films in different locations of Si/VO_2 all-dielectric nanodisks, we demonstrate different modulation amplitude of the electric or magnetic resonance scattering cross sections, leading to drastically different transmission spectrum upon VO_2 insulator to metal phase transition. The physical mechanism is originated from the field profiles of the resonance modes, which interact with VO_2 differently depending on its locations. Based on this mechanism, we experimentally demonstrated a large modulation of the transmittance from 82% to 28% at the 4.6 μm wavelength. Our work demonstrates a promising potential of VO_2-based active all-dielectric metasurface for mid-infrared photonic applications such as infrared camouflage, chemical/biomedical sensing, optical neuromorphic computing, and multispectral imaging.

https://doi.org/10.1364/PRJ.445571

1. INTRODUCTION

All-dielectric metasurfaces enabling light manipulation in two-dimensional photonic nanostructures have attracted great research interest recently. Compared to plasmonic devices, all-dielectric metasurfaces show characteristics of low optical absorption and unique Mie resonant modes [1–6]. A variety of novel photonic devices based on all-dielectric metasurfaces have been developed, including metalens [7–10], beam steerers [11–13], polarizers [14], and optical holography [15–21]. In the mid-infrared wavelength range, all-dielectric metasurfaces are promising for sensing, multispectral imaging, emissivity control, and infrared camouflage applications [22–27]. Nevertheless, most all-dielectric metasurfaces in the mid-infrared are static with fixed optical properties by design, which limit their application for tunable photonic devices.

Recently, active metasurfaces based on phase-change materials have attracted great research interest [28–37]. Phase-change materials such as $Ge_2Sb_2Te_5$ (GST) and VO_2 show large refractive index change ($\Delta n \approx 1$) in the visible to far-infrared wavelength range upon phase transition (PT). For GST, the large refractive index contrast is attributed to the nonvolatile process, which has been widely utilized for reconfigurable metasurfaces, including tunable color display [38], varifocal metalenses [7,39], beam-steering devices [40], switches [41], and tunable thermal absorbers [42], etc. Compared to GST, the PT process of VO_2 is volatile, which also shows much lower PT temperature than GST (68°C versus 600°C). Therefore, VO_2 is better fitted for the photonic devices requiring dynamic and continuous modulation. For instance, VO_2 has been applied for adaptive thermal camouflage [43], optical modulators

[34,44], and tunable absorbers/emitters [45,46]. Recently, VO_2-based active all-dielectric metasurfaces have been developed. VO_2 is either used as the only material to form Mie resonators, or incorporated in Si/VO_2 Mie resonators as the substrate or superstrate. Tunable Mie resonances based on VO_2 nanodisks in the visible wavelength range were reported [47]. Optical limiting effect based on Huygens' metasurfaces using VO_2/Si nanodisks was experimentally observed [4]. Amplitude or spectral tuning was demonstrated in VO_2/Si-based all-dielectric metasurfaces [48]. Apart from the phase change materials, other active materials are also employed to the reconfigurable metasurface devices, such as liquid crystal [49], graphene [50,51], InSb [52], and magnesium [53]. These devices show excellent tunability of the transmission spectrum in the visible to near-infrared, highlighting a promising potential for future device applications.

Here, we report a VO_2-based active all-dielectric metasurface in the mid-infrared wavelength range. Compared to previous reports, we made a step further by experimentally incorporating VO_2 thin films in different locations of a silicon nanodisk Mie resonator and demonstrated its tunable transmittance spectrum in the mid-infrared. We show experimentally and theoretically that the insulator to metal phase transition (IMT) of VO_2 influences the scattering cross section of Mie resonance modes differently, which strongly depends on the VO_2 film locations. By judiciously designing and fabricating VO_2 at the bottom or the middle of the Si Mie resonators, we show selective modulation of the scattering cross section of magnetic dipole or electric dipole resonances, respectively. We experimentally demonstrated a large modulation of the transmittance from 82% to 28% at 4.6 μm wavelength. These results indicate a promising potential of VO_2-based active metasurface for mid-infrared photonic device applications, such as infrared camouflage, chemical/biomedical sensing, optical neuromorphic computing, and multispectral imaging.

2. EXPERIMENTAL PROCEDURE

Figure 1(a) shows the schematic of the VO_2-based metasurfaces. The device consists of an array of hybrid α-Si/VO_2 nanodisks fabricated on a double side polished CaF_2 substrate. Two devices with VO_2 at different locations of the meta-atoms were fabricated, namely hybrid metasurface with VO_2 at the bottom of α-Si/HMB, and hybrid metasurface with VO_2 in the middle of α-Si/HMM, respectively. The hybrid Mie resonators were fabricated by e-beam lithography (EBL) and deep reactive ion etching (DRIE) after deposition of VO_2 and α-Si films on CaF_2, as shown Fig. 1(a) (see details in Appendix A). Figures 1(b) and 1(c) show the scanning electron microscope (SEM) images of the two fabricated devices. The period p of the nanodisks is 2.5 μm for both devices. The thickness t of VO_2 for both cases is 100 nm. The disk radius r for both metasurfaces is 0.62 μm. The height h for the HMB device is 0.9 μm, whereas the up and bottom silicon film thicknesses h_1 and h_2 for the HMM device are 570 nm and 330 nm, respectively.

3. RESULTS AND DISCUSSION

Figures 2(a) and 2(c) show the simulated transmittance spectra of the HMB and HMM. Considering the trapezoid shape of the fabricated nanodisks shown in Figs. 1(b) and 1(c), the structures of our simulation are optimized to well match with the experiment results. The spectrum shows two dips at 3.6 μm and 4.2 μm, corresponding to the electric dipole resonance (ED) and magnetic dipole resonance (MD) modes, respectively. We observe the disappearance of the MD mode at the wavelength of 4.2 μm when VO_2 changes from the dielectric to the metallic state, as shown in Fig. 2(a). For the ED mode, only a slight blueshift of the resonance peak and linewidth broadening are observed upon dielectric to metal phase transition. Figure 2(b) shows the transmittance spectra of the HMB device measured using a Fourier transform infrared (FTIR) spectrometer (see Appendix B), which matches with the simulation very well. For dielectric state VO_2, the ED and MD modes are observed at 3.7 μm and 4.2 μm wavelengths, respectively. After phase transition of VO_2 to the metallic state, the MD mode disappears and the ED mode shifts to a shorter wavelength of 3.6 μm with a broader linewidth, which are consistent with the simulation results. The results are quite different for the HMM device. Figure 2(c) shows the simulated transmittance spectra for the HMM device. The ED mode disappears when VO_2 changes from the dielectric to the metallic state, whereas the

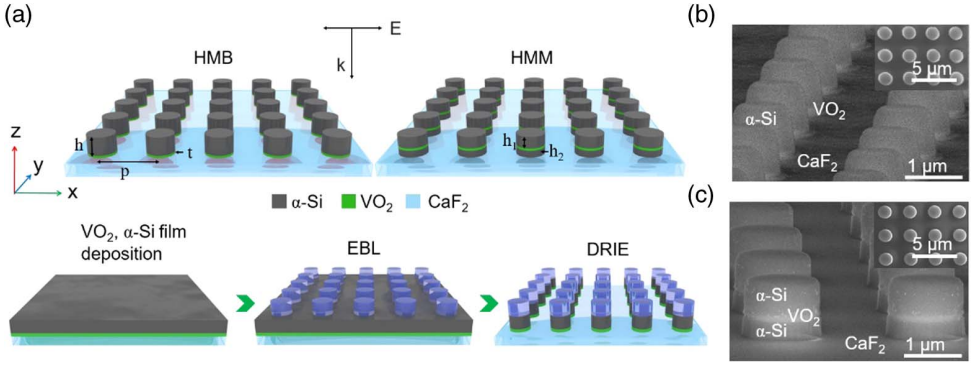

Fig. 1. Device structure and process flow. (a) Process flow and schematics of the two hybrid α-Si/VO_2 metasurfaces with VO_2 at the bottom and center of the α-Si nanodisks. SEM images of the (b) HMB and (c) HMM devices. Inset shows the top-view SEM image.

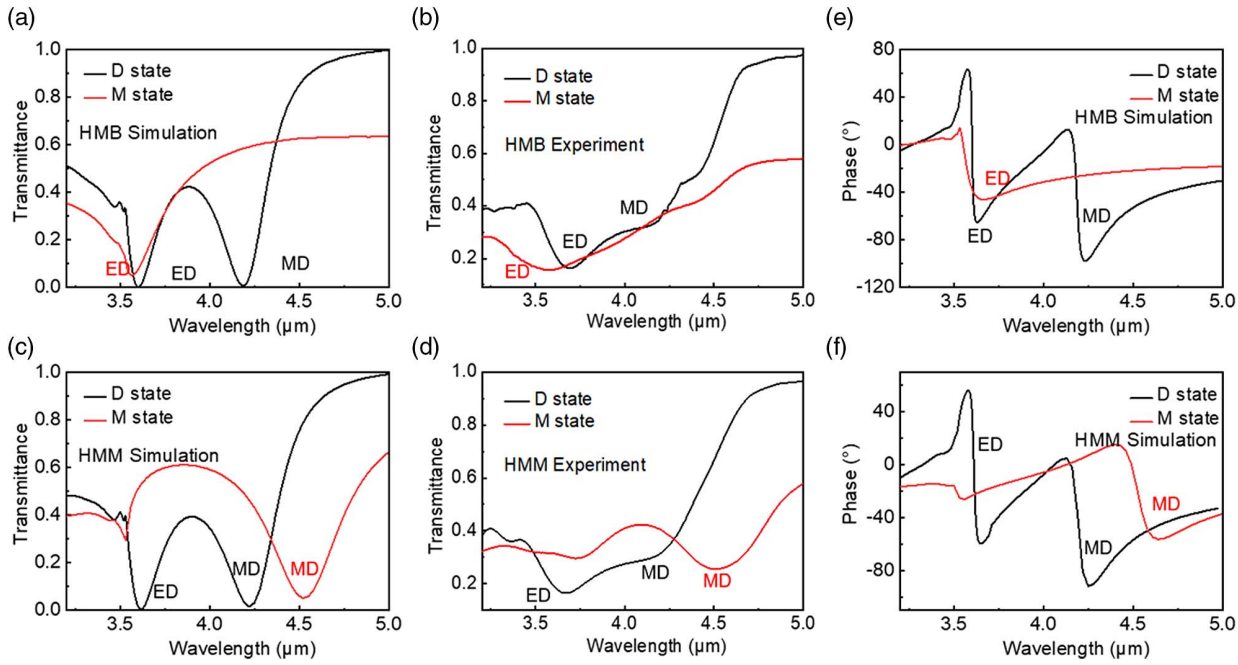

Fig. 2. Tunable optical properties of HMB and HMM configurations. (a) Simulated and (b) measured transmittance spectra of the HMB configuration at dielectric and metallic states. (c) Simulated and (d) measured transmittance spectra of HMM configuration at dielectric and metallic states. Simulated transmission phase spectra of (e) HMB and (f) HMM configurations at dielectric and metallic states.

MD mode remains. The resonance wavelength of the MD mode redshifts from 4.2 μm to 4.5 μm with a slight linewidth broadening. Figure 2(d) shows the measured transmittance spectra for the HMM device, which also match with the simulation results. Upon insulator to metal phase transition, the ED mode disappears, whereas the MD mode redshifts from 4.2 μm to 4.5 μm. Here, the shift of the MD upon phase transition in our experiment is comparable to the simulation results, demonstrating that VO_2 was not influenced by the etching process. Wavelength shift of the MD mode leads to a large intensity modulation amplitude from 82% to 28% at 4.6 μm wavelength. Interestingly, if we compare the transmittance spectra at the dielectric state for HMB and HMM samples, both in simulation and experiment, we notice they are almost the same. This is because VO_2 and α-Si show similar index of refraction at the mid-infrared wavelength range. Therefore, the transmittance spectrum shows little dependence on the VO_2 thin film location. However, after insulator to metal phase transition, the two samples show drastically different transmittance spectra. This result highlights that engineering the VO_2 film location in the meta-atom can significantly influence the optical property of the active metasurfaces. The simulated transmission phases of both metasurfaces are shown in Figs. 2(e) and 2(f). MD and ED resonances disappear for the HMB and HMM devices, respectively, resulting in clear phase modulation around the resonance wavelengths.

In order to study the mechanism of the active metasurface, near-field modal distributions of both the HMB and HMM devices are simulated, as shown in Fig. 3. Figure 3(a) shows the normalized electric field profiles of the ED mode at around 3.6 μm wavelength in the x–z plane of the HMB device. The color contour indicates the electric field profile. The white arrows indicate the electric field vector distribution. When VO_2 is at the dielectric state (left), the electric field is centered in the nanodisk and mostly points along the x direction. Only a small amount of the electric field is distributed in the VO_2 layer. Therefore, after IMT, the electric field becomes only slightly weaker in the Si nanoresonator, as shown by the right panel of Fig. 3(a). The higher absorption loss of the metallic VO_2 also causes a broader linewidth of the ED mode, as shown in Figs. 2(a) and 2(b). The case is different for the MD mode, as shown in Fig. 3(b). The electric field forms current loops which are largely confined in the VO_2 layer for the dielectric state. After IMT, the electric field is mostly absorbed by the metallic VO_2, as shown in the right panel of Fig. 3(b). The electric current loops disappear, causing the disappearance of the MD resonance mode. Similarly, we simulated the modal profiles of the HMM device, as shown in Figs. 3(c) and 3(d). When VO_2 is at the dielectric state [the left panels of Figs. 3(c) and 3(d)], the electric field distribution is similar to the HMB devices. This explains the similarity of the measured transmittance spectra between Figs. 2(b) and 2(d). However, when the VO_2 changes to the metallic state, the modal profile is very different for the HMM device. As shown by the right panel of Fig. 3(c), the electric field is strongly attenuated because VO_2 is located at the antinode of the electric field, causing the disappearance of the ED mode. For the MD mode shown in the right panel of Fig. 3(d), the electric field is only partly absorbed by the very thin VO_2 metallic film. The electric current loop and the MD mode still remain. The MD mode is redshifted due to a higher refractive index of the metallic VO_2. Similarly, due to the absorption loss of the metallic VO_2, a broader linewidth is observed for the MD mode, as shown in Figs. 2(c) and 2(d).

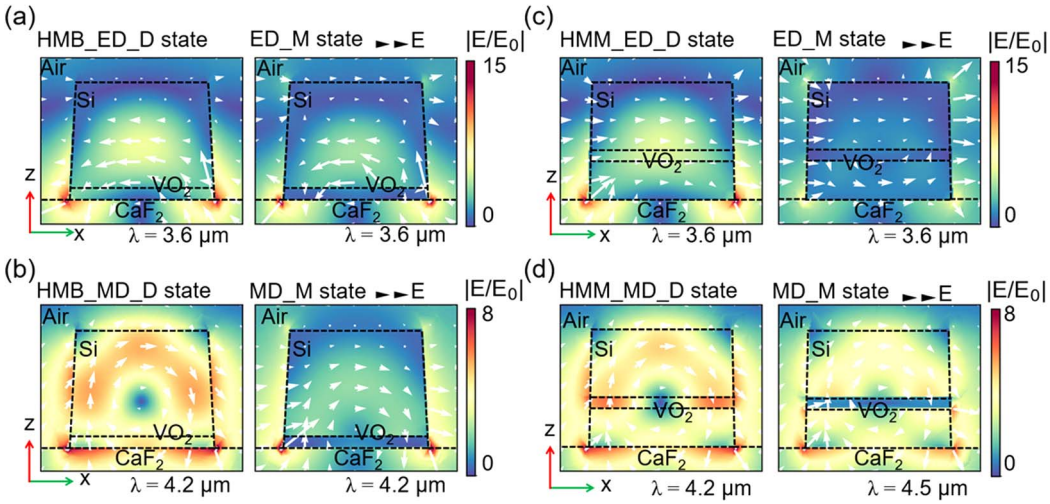

Fig. 3. Modal profiles of the HMB and HMM devices at ED and MD wavelengths, for both the dielectric state (D state) and the metallic state (M state). (a) Electric field distributions of ED mode at the dielectric state (left) and the metallic state (right) for the HMB device. (b) Electric field distributions of MD mode at the dielectric state (left) and the metallic state (right) for the HMB device. (c) Electric field distributions of the ED mode for the dielectric state (left) and the metallic state (right) of the HMM device. (d) Electric field distributions of MD mode for the dielectric state (left) and the metallic state (right) of the HMM device.

We further applied the multipolar decomposition method to analyze the scattering cross sections of the ED and MD modes [1]. The scattering cross sections are calculated based on the simulated polarization current in the Si/VO_2 nanoresonators using COMSOL Multiphysics (see Appendix C). Figure 4(a) shows the scattering cross section as a function of wavelength for the HMB device. For the dielectric state, the two peaks at 3.5 μm and 4.4 μm are mostly originated from electric and magnetic dipole scattering, respectively. For the metallic state, the ED scattering cross section decreases to 1/3 that of the dielectric state, whereas the MD scattering cross section almost disappears. For the HMM device, the scattering cross section is almost the same as the HMB device for the dielectric state, as shown in Fig. 4(b). For the metallic state,

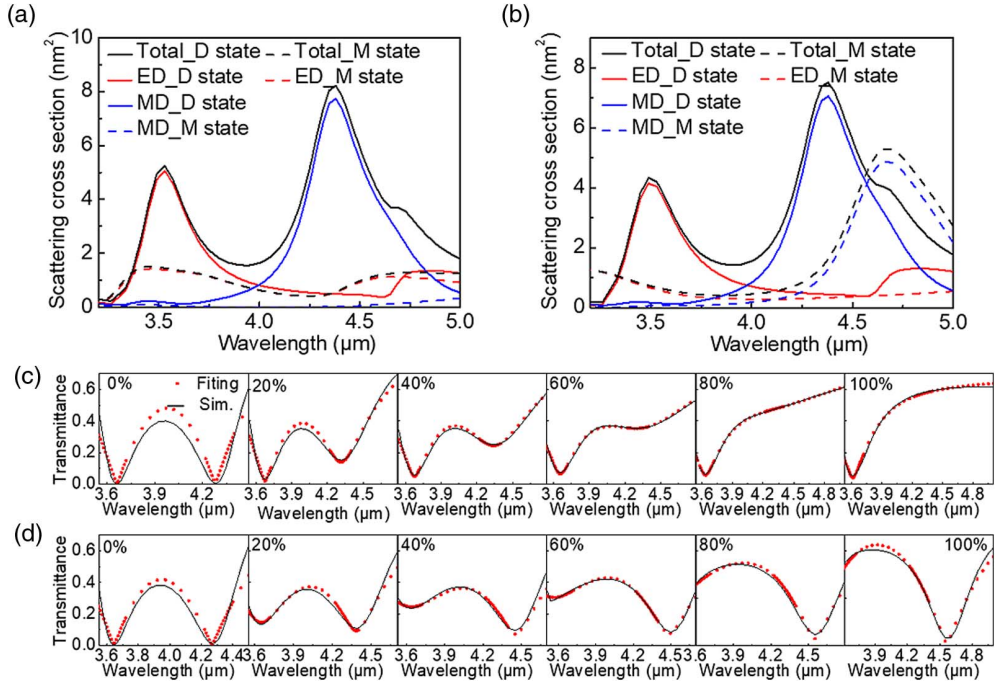

Fig. 4. Multipolar decomposition of the scattering cross sections. Scattering cross-section spectra of ED and MD modes of (a) HMB and (b) HMM configurations at the dielectric and metallic states. Simulated and fitted transmission spectra of (c) HMB and (d) HMM configurations for different metallic fractions of VO_2.

the MD scattering cross section decreases to 70% that of the dielectric state, whereas the ED scattering cross section disappears. We further used the temporal coupled-mode theory (TCMT) to analyze the evolution of the resonance modes during the phase transition. The transmittance can be determined as [54]

$$t = \frac{(j\omega - j\omega_1 + \Gamma_{i1})(j\omega - j\omega_2 + \Gamma_{i2}) + \kappa^2}{(j\omega - j\omega_1 + \Gamma_{i1} + \Gamma_{e1})(j\omega - j\omega_2 + \Gamma_{i2} + \Gamma_{e2}) + \kappa^2}, \tag{1}$$

where ω_1/ω_2, Γ_{e1}/Γ_{e2}, and Γ_{i1}/Γ_{i2} are the resonance angular frequencies, radiative decay rates, and nonradiative decay rates of the ED/MD modes, respectively. κ represents the direct coupling coefficient between the ED and MD modes. In Figs. 4(c) and 4(d), the fitted and simulated transmittance spectra for different metallic fractions of VO_2 are shown for both the HMB and HMM devices. The fitting parameters of the ED and MD modes are shown in Tables 1 and 2, respectively. Based on the characteristic parameters provided in Table 1, both the radiative (Γ_{e1}) and nonradiative (Γ_{i1}) decay rates of ED modes show small increase as the metallic fractions of VO_2 change from 0% to 100%, indicating a minor change in loss for both ED mode in HMB and MD mode in HMM devices. On the other hand, the radiative (Γ_{e2}) and nonradiative (Γ_{i2}) decay rates show large or weak enhancement, respectively, for the MD mode in the HMB device. Therefore, the disappearance of the MD mode is mainly attributed to the strong absorption of the metallic VO_2 layer. For the HMM device, according to the data in Table 2, the disappearance of the ED mode is also mainly attributed to the optical absorption loss of metallic VO_2. From the above analysis, we can conclude that placing VO_2 thin films at different locations of the meta-atoms causes selective absorption of different Mie resonance modes upon phase transition, leading to different transmittance spectrum of the metasurface.

Table 1. Fitting Parameters of the HMB Device

Metal Fraction	λ_1/μm	Γ_{i1}	λ_2/μm	Γ_{i2}	κ	Γ_{e1}	Γ_{e2}
0%	3.7	0	4.3	0	0	7.5	5.0
20%	3.7	0.2	4.3	1.2	0	8.5	5.8
40%	3.7	0.5	4.4	2.6	0	8.7	6.1
60%	3.7	0.8	4.4	5.4	0	8.5	7.0
80%	3.6	0.7	—	—	—	8.8	—
100%	3.6	0.5	—	—	—	7.7	—

Table 2. Fitting Parameters of the HMM Device

Metal Fraction	λ_1/μm	Γ_{i1}	λ_2/μm	Γ_{i2}	κ	Γ_{e1}	Γ_{e2}
0%	3.6	0	4.3	0	0	7.8	6.4
20%	3.6	2.1	4.4	0.8	0	10.8	5.5
40%	3.6	4.6	4.5	0.7	0	12.8	5.8
60%	3.6	5.4	4.5	0.8	0	10.8	6.8
80%	—	—	4.6	0.4	—	—	6.3
100%	—	—	4.6	0	—	—	7.6

4. CONCLUSION

In summary, we demonstrate a mid-infrared active metasurface based on Si/VO_2 hybrid nanoresonators. By incorporating VO_2 at the bottom or middle of α-Si nanoresonators, we show similar transmittance spectra of the two metasurfaces for the dielectric state, but drastically different transmittance spectra for the metallic state. Based on modal analysis, multipolar decomposition and TCMT fitting, we show that varying the location of VO_2 thin films induces different absorption loss of the Mie resonance modes, leading to almost independent tuning of the Mie resonance scattering cross sections for the ED and MD modes. The VO_2-based active all-dielectric metasurface is promising for mid-infrared photonic applications such as infrared camouflage, chemical/biomedical sensing, optical neuromorphic computing, and multispectral imaging.

APPENDIX A: SAMPLE FABRICATION

The Si/VO_2/SiO_2 multilayer thin films were deposited on double polished CaF_2 substrates by magnetron sputtering (Leybold, UNIVEX400CF), pulsed laser deposition (TSST), and plasma-enhanced chemical vapor deposition (PECVD, Trion). To promote adhesion, a 10 nm thick SiO_2 film was first deposited on the CaF_2 substrate by magnetron sputtering under 3.7 mTorr Ar ambient at room temperature. A 100 nm thick VO_2 thin film was then deposited on the SiO_2 film by pulsed laser deposition at room temperature using a 248 nm KrF excimer laser. The laser fluence was 3 J/cm^2. The deposition oxygen partial pressure was 14 mTorr. After deposition, the VO_2 film was crystallized by *in situ* annealing at 480°C temperature and under 1.2 Torr oxygen partial pressure for 1 h. The Si film was deposited on VO_2 by PECVD under 2.5 Torr SiH_4 ambient and at 300°C temperature.

The hybrid meta-atoms were fabricated by EBL and inductively coupled plasma-reactive ion etching (ICP-RIE). First, a 120 nm thick hydrogen silsesquioxane resist layer was spin-coated on the multilayer films with a spin speed of 4000 r/min. The sample was then baked on a hot plate for 1 min at 150°C. Then the nanodisk patterns were exposed by EBL using an acceleration voltage of 10 kV and an average dose of 2000 mC/cm^2. After exposure, the sample was developed in a mixed solution of NaOH/NaCl/H_2O (1/4/100) for 3 min and rinsed in de-ionized water for 1 min. After that, the top Si film was first etched in Cl_2 plasma in an ICP-RIE system under 7.5 mTorr pressure. The powers of ICP and RIE were 500 W and 40 W, respectively. Finally, the VO_2 film was etched in a SF_6, CHF_3, and O_2 plasma mixture under 35 mTorr pressure with an RIE power of 20 W.

APPENDIX B: OPTICAL CHARACTERIZATION

The transmission spectra were measured by an FTIR spectrometer (Perkin Elmer) equipped with a reflective focusing infrared microscope (Spotlight 2000i). The spot size was 100 μm × 100 μm. To induce the phase transition of VO_2, a hot plate was used to heat the sample in the 20°C–100°C temperature range.

APPENDIX C: SIMULATION AND MULTIPOLAR DECOMPOSITION

The simulation of the transmittance spectra and near-field modal profiles was performed using the commercial software COMSOL Multiphysics. Periodic boundary conditions were used around the nanodisks. The port boundary condition was used to define the polarization and angle of incidence. To avoid the effect of scattered light, a perfectly matched layer was set at the top and bottom layers near the port. The transmittance spectra were calculated using the simulated S parameters in COMSOL. The optical constants of VO_2 were adopted from Ref. [55]. The index of α-Si was set to 3.4.

To perform multipolar decomposition, we calculated the scattering field of the nanodisks embedded in a homogeneous medium using COMSOL. 3 × 3 periodic nanodisks were used in our simulation to resemble the scattering field of the periodic nanodisks. The total electric fields were extracted from COMSOL, and the displacement current was defined as

$$J(r) = -i\omega[\varepsilon(r) - \varepsilon_b]E_{\text{total}}(r), \tag{C1}$$

where $\varepsilon(r)$ is the permittivity of the nanodisks, ε_b is the permittivity of the surrounding host medium, and $E_{\text{total}}(r)$ is the total electric field inside the nanodisks. According to the multipolar decomposition theory, the electric and magnetic multipole coefficients $a(\ell, m)$ and $b(\ell, m)$ are defined as [1]

$$\begin{aligned} a(\ell,m) = {} & \frac{(-i)^{\ell-1}k\eta}{2\pi E_0}\frac{\sqrt{(\ell-m)!}}{\sqrt{\ell(\ell+1)(\ell+m)!}}\int \exp(-im\phi) \\ & \times\left\{[\psi_l'(kr)+\psi_l(kr)]P_l^m(\cos\theta)\hat{r}\cdot J(r)\right. \\ & +\frac{\psi_l'(kr)}{kr}\left[\frac{\mathrm{d}}{\mathrm{d}\theta}P_l^m(\cos\theta)\hat{\theta}\cdot J(r)\right. \\ & \left.\left.-\frac{im}{\sin\theta}P_l^m(\cos\theta)\hat{\phi}\cdot J(r)\right]\right\}\mathrm{d}^3r, \end{aligned} \tag{C2}$$

$$\begin{aligned} b(\ell,m) = {} & \frac{(-i)^{\ell+1}k^2\eta}{2\pi E_0}\frac{\sqrt{(\ell-m)!}}{\sqrt{\ell(\ell+1)(\ell+m)!}}\int \exp(-im\phi)j_\ell(kr) \\ & \times\left[\frac{im}{\sin\theta}P_l^m(\cos\theta)\hat{\theta}\cdot J(r)+\frac{\mathrm{d}}{\mathrm{d}\theta}P_l^m(\cos\theta)\hat{\phi}\cdot J(r)\right], \end{aligned} \tag{C3}$$

where E_0 is the electric field of the incident light, $j_l(kr)$ is the first kind Bessel function and $P_l^m(\cos\theta)$ is the Legendre polynomials. Therefore, the scattering cross sections of the electric multipole C_{scatE} and magnetic multipole C_{scatM} are defined as

$$C_{\text{scatE}} = \frac{\pi}{k^2}\sum_{\ell=1}^{\infty}\sum_{m=-\ell}^{l}(2\ell+1)|a(\ell,m)|^2, \tag{C4}$$

$$C_{\text{scatM}} = \frac{\pi}{k^2}\sum_{\ell=1}^{\infty}\sum_{m=-\ell}^{l}(2\ell+1)|b(\ell,m)|^2. \tag{C5}$$

Funding. Ministry of Science and Technology of the People's Republic of China (MOST) (2018YFE0109200); National Natural Science Foundation of China (NSFC) (51972044, 52021001); Sichuan Provincial Science and Technology Department (2019YFH0154, 2020ZYD015); Open-Foundation of Key Laboratory of Laser Device Technology, China North Industries Group Corporation Limited (KLLDT202003); Fundamental Research Funds for the Central Universities (ZYGX2020J005); Foundation of CAEP Ultra-precision Machining Technology Key Laboratory (ZM18008); Open Project Program of State Key Laboratory of Vanadium and Titanium Resources Comprehensive Utilization (2021P4FZG08A).

Acknowledgment. L. B. and T. K. conceived and designed the experiment. T. K. and B. F. performed the sample fabrication, and L. B. and J. Q. supervised the project. All authors discussed the research.

Disclosures. The authors declare no competing interest.

Data Availability. The data used to support the findings of this study are available from the corresponding author upon request.

[†]These authors contributed equally to this paper.

REFERENCES

1. J. Tian, H. Luo, Y. Yang, F. Ding, Y. Qu, D. Zhao, M. Qiu, and S. I. Bozhevolnyi, "Active control of anapole states by structuring the phase-change alloy $Ge_2Sb_2Te_5$," Nat. Commun. **10**, 396 (2019).
2. D. R. Abujetas, Á. Barreda, F. Moreno, A. Litman, J. M. Geffrin, and J. A. Sánchez-Gil, "High-*Q* transparency band in all-dielectric metasurfaces induced by a quasi bound state in the continuum," Laser Photonics Rev. **15**, 2000263 (2021).
3. H. M. Doeleman, F. Monticone, W. Den Hollander, A. Alù, and A. F. Koenderink, "Experimental observation of a polarization vortex at an optical bound state in the continuum," Nat. Photonics **12**, 397–401 (2018).
4. A. Howes, Z. Zhu, D. Curie, J. R. Avila, V. D. Wheeler, R. F. Haglund, and J. G. Valentine, "Optical limiting based on Huygens' metasurfaces," Nano Lett. **20**, 4638–4644 (2020).
5. A. Howes, W. Wang, I. Kravchenko, and J. Valentine, "Dynamic transmission control based on all-dielectric Huygens metasurfaces," Optica **5**, 787–792 (2018).
6. S. Yuan, X. Qiu, C. Cui, L. Zhu, Y. Wang, Y. Li, J. Song, Q. Huang, and J. Xia, "Strong photoluminescence enhancement in all-dielectric Fano metasurface with high quality factor," ACS Nano **11**, 10704–10711 (2017).
7. M. Y. Shalaginov, S. An, Y. Zhang, F. Yang, P. Su, V. Liberman, J. B. Chou, C. M. Roberts, M. Kang, C. Rios, Q. Du, C. Fowler, A. Agarwal, K. A. Richardson, C. Rivero-Baleine, H. Zhang, J. Hu, and T. Gu, "Reconfigurable all-dielectric metalens with diffraction-limited performance," Nat. Commun. **12**, 1225 (2021).
8. S. Gao, C. S. Park, C. Zhou, S. S. Lee, and D. Y. Choi, "Twofold polarization-selective all-dielectric trifoci metalens for linearly polarized visible light," Adv. Opt. Mater. **7**, 1900883 (2019).
9. C. Schlickriede, S. S. Kruk, S. S. Kruk, L. Wang, B. Sain, Y. Kivshar, and T. Zentgraf, "Nonlinear imaging with all-dielectric metasurfaces," Nano Lett. **20**, 4370–4376 (2020).
10. L. Yu, Y. Fan, Y. Wang, C. Zhang, W. Yang, Q. Song, and S. Xiao, "Spin angular momentum controlled multifunctional all-dielectric metasurface doublet," Laser Photonics Rev. **14**, 1900324 (2020).
11. S. Q. Li, X. Xu, R. M. Veetil, V. Valuckas, R. Paniagua-Domínguez, and A. I. Kuznetsov, "Phase-only transmissive spatial light modulator based on tunable dielectric metasurface," Science **364**, 1087–1090 (2019).
12. T. Shi, Y. Wang, Z. L. Deng, X. Ye, Z. Dai, Y. Cao, B. O. Guan, S. Xiao, and X. Li, "All-dielectric kissing-dimer metagratings for asymmetric high diffraction," Adv. Opt. Mater. **7**, 1901389 (2019).

13. P. C. Wu, R. A. Pala, G. Kafaie Shirmanesh, W. H. Cheng, R. Sokhoyan, M. Grajower, M. Z. Alam, D. Lee, and H. A. Atwater, "Dynamic beam steering with all-dielectric electro-optic III–V multiple-quantum-well metasurfaces," Nat. Commun. **10**, 3654 (2019).
14. S. Wang, Z. L. Deng, Y. Wang, Q. Zhou, X. Wang, Y. Cao, B. O. Guan, S. Xiao, and X. Li, "Arbitrary polarization conversion dichroism metasurfaces for all-in-one full Poincaré sphere polarizers," Light Sci. Appl. **10**, 24 (2021).
15. G. Qu, W. Yang, Q. Song, Y. Liu, C. W. Qiu, J. Han, D. P. Tsai, and S. Xiao, "Reprogrammable meta-hologram for optical encryption," Nat. Commun. **11**, 5484 (2020).
16. S. Sun, W. Yang, C. Zhang, J. Jing, Y. Gao, X. Yu, Q. Song, and S. Xiao, "Real-time tunable colors from microfluidic reconfigurable all-dielectric metasurfaces," ACS Nano **12**, 2151–2159 (2018).
17. X. Zhang, Q. Wang, Q. Xu, X. Zhang, C. Tian, Y. Xu, J. Gu, Z. Tian, C. Ouyang, J. Han, and W. Zhang, "All-dielectric meta-holograms with holographic images transforming longitudinally," ACS Photonics **5**, 599–606 (2018).
18. M. A. Ansari, I. Kim, D. Lee, M. H. Waseem, M. Zubair, N. Mahmood, T. Badloe, S. Yerci, T. Tauqeer, M. Q. Mehmood, and J. Rho, "A spin-encoded all-dielectric metahologram for visible light," Laser Photonics Rev. **13**, 1900065 (2019).
19. B. Reineke, B. Sain, R. Zhao, L. Carletti, B. Liu, L. Huang, C. De Angelis, and T. Zentgraf, "Silicon metasurfaces for third harmonic geometric phase manipulation and multiplexed holography," Nano Lett. **19**, 6585–6591 (2019).
20. X. Guo, P. Li, J. Zhong, S. Liu, B. Wei, W. Zhu, S. Qi, H. Cheng, and J. Zhao, "Tying polarization-switchable optical vortex knots and links via holographic all-dielectric metasurfaces," Laser Photonics Rev. **14**, 1900366 (2020).
21. Q. Wei, B. Sain, Y. Wang, B. Reineke, X. Li, L. Huang, and T. Zentgraf, "Simultaneous spectral and spatial modulation for color printing and holography using all-dielectric metasurfaces," Nano Lett. **19**, 8964–8971 (2019).
22. K. Tang, X. Wang, K. Dong, Y. Li, J. Li, B. Sun, X. Zhang, C. Dames, C. Qiu, J. Yao, and J. Wu, "A thermal radiation modulation platform by emissivity engineering with graded metal–insulator transition," Adv. Mater. **32**, 1907071 (2020).
23. L. Long, S. Taylor, and L. Wang, "Enhanced infrared emission by thermally switching the excitation of magnetic polariton with scalable microstructured VO_2 metasurfaces," ACS Photonics **7**, 2219–2227 (2020).
24. K. Tang, K. Dong, C. J. Nicolai, Y. Li, J. Li, S. Lou, C. W. Qiu, D. H. Raulet, J. Yao, and J. Wu, "Millikelvin-resolved ambient thermography," Sci. Adv. **6**, eabd8688 (2020).
25. H. Zuo, D. Y. Choi, X. Gai, P. Ma, L. Xu, D. N. Neshev, B. Zhang, and B. Luther-Davies, "High-efficiency all-dielectric metalenses for mid-infrared imaging," Adv. Opt. Mater. **5**, 1700585 (2017).
26. C. Yan, X. Li, M. Pu, X. Ma, F. Zhang, P. Gao, K. Liu, and X. Luo, "Midinfrared real-time polarization imaging with all-dielectric metasurfaces," Appl. Phys. Lett. **114**, 161904 (2019).
27. T. Lewi, N. A. Butakov, and J. A. Schuller, "Thermal tuning capabilities of semiconductor metasurface resonators," Nanophotonics **8**, 331–338 (2018).
28. S. An, C. Fowler, B. Zheng, M. Y. Shalaginov, H. Tang, H. Li, L. Zhou, J. Ding, A. M. Agarwal, C. Rivero-Baleine, K. A. Richardson, T. Gu, J. Hu, and H. Zhang, "A deep learning approach for objective-driven all-dielectric metasurface design," ACS Photonics **6**, 3196–3207 (2019).
29. C. H. Chu, M. L. Tseng, J. Chen, P. C. Wu, Y. H. Chen, H. C. Wang, T. Y. Chen, W. T. Hsieh, H. J. Wu, G. Sun, and D. P. Tsai, "Active dielectric metasurface based on phase-change medium," Laser Photonics Rev. **10**, 986–994 (2016).
30. A. Leitis, A. Heßler, S. Wahl, M. Wuttig, T. Taubner, A. Tittl, and H. Altug, "All-dielectric programmable Huygens' metasurfaces," Adv. Funct. Mater. **30**, 1910259 (2020).
31. S. Abdollahramezani, O. Hemmatyar, M. Taghinejad, H. Taghinejad, Y. Kiarashinejad, M. Zandehshahvar, T. Fan, S. Deshmukh, A. A. Eftekhar, W. Cai, E. Pop, M. A. El-Sayed, and A. Adibi, "Dynamic hybrid metasurfaces," Nano Lett. **21**, 1238–1245 (2021).
32. Y. Wang, P. Landreman, D. Schoen, K. Okabe, A. Marshall, U. Celano, H. S. P. Wong, J. Park, and M. L. Brongersma, "Electrical tuning of phase-change antennas and metasurfaces," Nat. Nanotechnol. **16**, 667–672 (2021).
33. Y. Zhang, C. Fowler, J. Liang, B. Azhar, M. Y. Shalaginov, S. Deckoff-Jones, S. An, J. B. Chou, C. M. Roberts, V. Liberman, M. Kang, C. Ríos, K. A. Richardson, C. Rivero-Baleine, T. Gu, H. Zhang, and J. Hu, "Electrically reconfigurable non-volatile metasurface using low-loss optical phase-change material," Nat. Nanotechnol. **16**, 661–666 (2021).
34. Y. Kim, P. C. Wu, R. Sokhoyan, K. Mauser, R. Glaudell, G. Kafaie Shirmanesh, and H. A. Atwater, "Phase modulation with electrically tunable vanadium dioxide phase-change metasurfaces," Nano Lett. **19**, 3961–3968 (2019).
35. B. Gholipour, A. Karvounis, J. Yin, C. Soci, K. F. MacDonald, and N. I. Zheludev, "Phase-change-driven dielectric-plasmonic transitions in chalcogenide metasurfaces," NPG Asia Mater. **10**, 533–539 (2018).
36. C. Ruiz De Galarreta, I. Sinev, A. M. Arseny, P. Trofimov, K. Ladutenko, S. G.-C. Carrillo, E. Gemo, A. Baldycheva, J. Bertolotti, and C. D. Wright, "Reconfigurable multilevel control of hybrid all-dielectric phase-change metasurfaces," Optica **7**, 476–484 (2020).
37. M. N. Julian, C. Williams, S. Borg, S. Bartram, and H. J. Kim, "Reversible optical tuning of GeSbTe phase-change metasurface spectral filters for mid-wave infrared imaging," Optica **7**, 746–754 (2020).
38. S. G. C. Carrillo, L. Trimby, Y. Y. Au, V. K. Nagareddy, G. Rodriguez-Hernandez, P. Hosseini, C. Ríos, H. Bhaskaran, and C. D. Wright, "A nonvolatile phase-change metamaterial color display," Adv. Opt. Mater. **7**, 1801782 (2019).
39. X. Yin, T. Steinle, L. Huang, T. Taubner, M. Wuttig, T. Zentgraf, and H. Giessen, "Beam switching and bifocal zoom lensing using active plasmonic metasurfaces," Light Sci. Appl. **6**, e17016 (2017).
40. C. R. de Galarreta, A. M. Alexeev, Y. Y. Au, M. Lopez-Garcia, M. Klemm, M. Cryan, J. Bertolotti, and C. D. Wright, "Nonvolatile reconfigurable phase-change metadevices for beam steering in the near infrared," Adv. Funct. Mater. **28**, 1704993 (2018).
41. A. Ahmadivand, B. Gerislioglu, R. Sinha, M. Karabiyik, and N. Pala, "Optical switching using transition from dipolar to charge transfer plasmon modes in $Ge_2Sb_2Te_5$ bridged metallodielectric dimers," Sci. Rep. **7**, 42807 (2017).
42. A. Tittl, A. K. U. Michel, M. Schäferling, X. Yin, B. Gholipour, L. Cui, M. Wuttig, T. Taubner, F. Neubrech, and H. Giessen, "A switchable mid-infrared plasmonic perfect absorber with multispectral thermal imaging capability," Adv. Mater. **27**, 4597–4603 (2015).
43. S. Chandra, D. Franklin, J. Cozart, A. Safaei, and D. Chanda, "Adaptive multispectral infrared camouflage," ACS Photonics **5**, 4513–4519 (2018).
44. P. Guo, M. S. Weimer, J. D. Emery, B. T. Diroll, X. Chen, A. S. Hock, R. P. H. Chang, A. B. F. Martinson, and R. D. Schaller, "Conformal coating of a phase change material on ordered plasmonic nanorod arrays for broadband all-optical switching," ACS Nano **11**, 693–701 (2017).
45. K. Sun, C. A. Riedel, A. Urbani, M. Simeoni, S. Mengali, M. Zalkovskij, B. Bilenberg, C. H. De Groot, and O. L. Muskens, "VO_2 thermochromic metamaterial-based smart optical solar reflector," ACS Photonics **5**, 2280–2286 (2018).
46. J. Rensberg, S. Zhang, Y. Zhou, A. S. McLeod, C. Schwarz, M. Goldflam, M. Liu, J. Kerbusch, R. Nawrodt, S. Ramanathan, D. N. Basov, F. Capasso, C. Ronning, and M. A. Kats, "Active optical metasurfaces based on defect-engineered phase-transition materials," Nano Lett. **16**, 1050–1055 (2016).
47. P. Kepič, F. Ligmajer, M. Hrtoň, H. Ren, L. D. S. Menezes, S. A. Maier, and T. Šikola, "Optically tunable Mie resonance VO_2 nanoantennas for metasurfaces in the visible," ACS Photonics **8**, 1048–1057 (2021).
48. A. Tripathi, J. John, S. Kruk, Z. Zhang, H. S. Nguyen, L. Berguiga, P. R. Romeo, R. Orobtchouk, S. Ramanathan, Y. Kivshar, and S. Cueff, "Tunable Mie-resonant dielectric metasurfaces based on VO_2 phase-transition materials," ACS Photonics **8**, 1206–1213 (2021).
49. Y. Hu, X. Ou, T. Zeng, J. Lai, J. Zhang, X. Li, X. Luo, L. Li, F. Fan, and H. Duan, "Electrically tunable multifunctional polarization-dependent metasurfaces integrated with liquid crystals in the visible region," Nano Lett. **21**, 4554–4562 (2021).

50. B. Zeng, Z. Huang, A. Singh, Y. Yao, A. K. Azad, A. D. Mohite, A. J. Taylor, D. R. Smith, and H. T. Chen, "Hybrid graphene metasurfaces for high-speed mid-infrared light modulation and single-pixel imaging," Light Sci. Appl. **7**, 51 (2018).
51. M. C. Sherrott, P. W. C. Hon, K. T. Fountaine, J. C. Garcia, S. M. Ponti, V. W. Brar, L. A. Sweatlock, and H. A. Atwater, "Experimental demonstration of >230° phase modulation in gate-tunable graphene-gold reconfigurable mid-infrared metasurfaces," Nano Lett. **17**, 3027–3034 (2017).
52. P. P. Iyer, M. Pendharkar, C. J. Palmstrøm, and J. A. Schuller, "Ultrawide thermal free-carrier tuning of dielectric antennas coupled to epsilon-near-zero substrates," Nat. Commun. **8**, 472 (2017).
53. J. Li, Y. Chen, Y. Hu, H. Duan, and N. Liu, "Magnesium-based metasurfaces for dual-function switching between dynamic holography and dynamic color display," ACS Nano **14**, 7892–7898 (2020).
54. C. Li, W. Zhu, Z. Liu, R. Pan, S. Hu, S. Du, J. Li, and C. Gu, "Independent tuning of bright and dark meta-atoms with phase change materials on EIT metasurfaces," Nanoscale **12**, 10065–10071 (2020).
55. L. Yang, "Thermal tuning intelligent infrared absorber," MS thesis (University of Electronic Science and Technology of China, 2017).